Journal of Alloys and Compounds 976 (2024) 173195

Contents lists available at ScienceDirect

Journal of Alloys and Compounds

journal homepage: www.elsevier.com/locate/jalcom

Phase equilibria and crystal structures in the ytterbium–copper–zinc system

F. Akbar [a], I. Čurlík [b], M. Reiffers [b], M. Giovannini [a,*]

[a] Department of Chemistry and Industrial Chemistry, University of Genova, Via Dodecaneso 31, 16146 Genova, Italy
[b] Faculty of Humanities and Natural Sciences, University of Presov, 17. novembra 1, 08001 Presov, Slovakia

ARTICLE INFO

Keywords:
Rare earth alloys and compounds
Magnetic properties
Crystal structures

ABSTRACT

Phase equilibria in the isothermal section (600 °C) of the ytterbium-copper-zinc ternary system were determined over the entire concentration range by powder X-ray diffraction and scanning electron microscopy with energy-dispersive X-ray spectroscopy. Extended substitutional Cu/Zn homogeneity regions are mainly formed from the Yb-Zn and Yb-Cu binary compounds. There are four ternary compounds, namely τ_1-$YbCu_{5-x}Zn_x$ (cubic $AuBe_5$ type, $0.7 < x \leq 1.5$), τ_2-$YbCu_{5-x}Zn_x$ (hexagonal $CaCu_5$ type, $1.8 \leq x \leq 4.4$), τ_3-Yb_2CuZn_7 and τ_4-$Yb_5Cu_{2-x}Zn_{1+x}$. Magnetic measurements were performed for compositions along the phases τ_1-$YbCu_{5-x}Zn_x$ and τ_2-$YbCu_{5-x}Zn_x$, as well as for the compound $Yb_{33}Cu_{50}Zn_{17}$ belonging to the pseudobinary system $YbCu_2$-$YbZn_2$. While the Yb ion has a valence of 2 + for compositions ≥33% at% Yb, the Yb valence along the $YbCu_{5-x}Zn_x$ composition line is influenced by the crystal structure: Yb^{3+} for the cubic $AuBe_5$ type and nonmagnetic Yb^{2+} for the hexagonal $CaCu_5$ type.

1. Introduction

Ternary intermetallic compounds $R_xT_yM_z$ formed by R = Yb, Ce with T = transition metal and M = transition or p-block element have been extensively studied because of their unusual physical properties ranging from heavy fermion behavior, intermediate valence and Kondo interactions due to hybridization between 4 f and conduction electrons [1,2]. Recently, special emphasis has been placed on the study of $YbCu_{5-x}M_x$ solid solutions crystallizing in the cubic $AuBe_5$ structure for M = Au, Ag, In [3–5] and in the hexagonal $CaCu_5$ structure for M = Al and Ga [6,7]. In these cases, the substitution of Cu by M offers the possibility to investigate the different evolution of the ground state properties depending on the element M.

In both cases of crystal structure, there are remarkable examples of intriguing physical properties. In the case of the cubic $YbCu_{5-x}Au_x$ system, Cu/Au substitution drives the system through a quantum critical point (QCP) at $x = 0.4$ [3] from a nonmagnetic to a magnetic ground state, while in the case of hexagonal $YbCu_{5-x}Al_x$ the driving force for the QCP at $x = 1.5$ is a change in valence from $\nu \approx 2.2(x = 0)$ to $\nu = 3(x = 2)$ [6].

The interest in cubic solid solutions was stimulated by the study of the heavy fermions $YbCu_4M$ with M = Ag, and Au [8] which crystallize in the cubic $MgCu_4Sn$ prototype (ordered structure derivative of $AuBe_5$, sp. gr. $F\bar{4}3m$), which were initially considered as stoichiometric compounds but later showed more or less extended homogeneity regions. A study of other heavy fermions extended the members of the cubic structure to M = Cd, Mg, Tl, and Zn, of which $YbCu_4Zn$ [9] seems to be the most interesting. Similar to $YbCu_{4.6}Au_{0.4}$ [3], an increase in C_P/T and resistivity is observed at low temperatures, while no magnetic order is found above 100 mK [9]. Since no data on the existence of $YbCu_{5-x}Zn_x$ solid solutions can be found in the literature, a study on this topic provided the impetus to investigate the phase diagram of the Yb-Cu-Zn system.

In this work, the phase equilibria of the Yb-Cu-Zn ternary system studied at 600 °C are described in detail, with the main aim of searching for new intermetallic compounds. Particular attention is paid to $YbCu_{5-x}Zn_x$, which exhibits either the cubic or hexagonal crystal structure in different compositional ranges. In addition, the physical properties of selected compositions of $YbCu_{5-x}Zn_x$ and $Yb_{33}Cu_{17}Zn_{50}$ are discussed.

2. Literature data

2.1. Binary boundary systems

The Yb–Cu phase diagram determined by Iandelli and Palenzona [10] was further investigated by Subramanian and Laughlin [11] and more recently by Giovannini et al. [12] in the range of 10 to 24 at%.

* Correspondence to: Department of Chemistry and Industrial Chemistry, University of Genova, Via Dodecaneso 31, I-16146 Genova, Italy.
E-mail address: mauro.giovannini@unige.it (M. Giovannini).

https://doi.org/10.1016/j.jallcom.2023.173195
Received 26 July 2023; Received in revised form 13 December 2023; Accepted 13 December 2023
Available online 15 December 2023

Table 1
Crystal structure data of ternary compositions present in the Yb–Cu–Zn system.

Phase	Pearson symbol/prototype	Lattice parameters (nm)			Ref.
		a	*b*	*c*	
YbCuZn	Orthorhombic *oI*12-KHg_2	0.4432(2)	0.7088(3)	0.7501(3)	[18]
$YbCu_4Zn$	Cubic *cF*24-$MgCu_4Sn$	0.7046			[9]
Yb_5Cu_2Zn	Tetragonal *tI*32-Mo_5B_2Si	0.7766(1)		1.4533(2)	[19]

According to the most recent studies, there are five binary phases: YbCu (FeB-type, peritectic formation at 628 °C), $YbCu_2$ (KHg_2-type, peritectic formation at 760 °C), $YbCu_{3.5}$ (monoclinic superstructure of the $AuBe_5$-type, peritectic formation at 825 °C), $YbCu_{4.5}$ (monoclinic superstructure of $AuBe_5$-type, congruent formation at 935 °C) and $YbCu_{6.5}$ (related to the $CaCu_5$-type, peritectic formation at 870 °C) [12]. The compound $YbCu_5$, cubic $AuBe_5$-type and prototype of the cubic $YbCu_{5-x}M_x$ solid solutions, forms only under high pressure [12].

The Cu–Zn system was investigated by Argent and Wakeman [13], and later assessed by Massalski [14]. At 600 °C the stable phases and their homogeneity ranges, starting from the Cu side, are the following: (Cu) formed up to 37 at% Zn, β (W-type) from 43 to 50 at% Zn, γ (Cu_5Zn_8-type) from 58 to 70 at% Zn, δ (W-type) from 74 to 77 at% Zn and liquid phase (L) from 87 at% to 100 at% Zn.

The Yb–Zn phase diagram, which was investigated by Mason and Chiotti [15], consists of six phases: YbZn (CsCl-type, melts congruently at 650 °C), $YbZn_2$ (α$YbZn_2$, KHg_2-type, stable up to 645 °C, melts congruently at 751 °C), Yb_3Zn_{11} (La_3Al_{11}-type, melts peritectically at 695 °C), $Yb_{13}Zn_{58}$ ($Gd_{13}Zn_{58}$-type, melts congruently at 752 °C), Yb_2Zn_{17} (Th_2Zn_{17}-type, melts congruently at 754 °C) and $YbZn_{11}$ ($BaCd_{11}$-type, melts congruently at 755 °C). $YbZn_2$ occurs in two polymorphic forms: α$YbZn_2$ (below 645 °C) and β$YbZn_2$ (between 645–751 °C). Other authors report the existence of the intermediate phase Yb_3Zn_{17} (Ru_3Be_{17} prototype, space group $Im\bar{3}$) [16,17].

2.1.1. *Yb-Cu-Zn ternary system*

There is no data on the existence of phase equilibria in the Yb–Cu–Zn ternary system. Three ternary compositions are known from the literature and are listed in Table 1.

The compound YbCuZn, prepared by Fornasini *et al.*, crystallizes in the orthorhombic KHg_2 structure type (sp. gr. *Imma*). A comparison of the ionic radius between *R*CuZn (*R* = rare-earth metal) results in a higher value for YbCuZn, which indicates a divalent behavior of the Yb ion. The physical properties of this compound have not yet been investigated [18].

The compound $YbCu_4Zn$, described by Sarrao *et al.*, crystallizes in the cubic $MgCu_4Sn$-type structure (sp. gr. $F\bar{4}3m$). Specific heat studies show an upward trend of C_P/T at low temperatures which could indicate magnetic ordering. Electrical resistivity measurements also show an increase at low temperatures, which is suppressed by applying a high magnetic field (300 kOe) [9].

The compound Yb_5Cu_2Zn was synthesized by Tappe *et al.* [19] and its structure was investigated using the XRD technique. The compound belongs to the series of M_5T_2X intermetallic compounds with a tetragonal crystal structure of Mo_5B_2Si-type (sp. gr. *I4/mcm*) where *M* = rare earth metal, T = transition metal and X = transition/p-block element. Magnetic susceptibility measurements on the compound yielded small absolute susceptibility $\chi(T)$ values indicating the presence of nonmagnetic Yb^{2+} ions.

3. Experimental work

The elements selected for the preparation of the alloys, copper (pieces, 99.99% mass purity, NewMet Koch, Waltham Abbey, Essex, UK), zinc (ingots, 99.999% mass purity, NewMet Koch, Waltham Abbey, UK), and ytterbium (pieces, 99.9% mass purity, MaTecK, Julich, Germany), were weighed in a total amount of 0.7–1.0 g and enclosed by arc welding in tantalum crucibles in an argon atmosphere to minimize material loss. The crucibles were placed in an induction furnace and heated under a continuous supply of pure argon. The samples were shaken at intervals during heating to achieve homogeneous melting of the alloys and then sealed in quartz. Annealing of the samples was carried out in a resistance furnace at 600 °C/10 days, after which the samples were quenched with cold water. The total mass losses during synthesis and annealing did not exceed 0.5%.

For the characterization of the samples by scanning electron microscopy (SEM) equipped with an energy-dispersive X-ray spectroscopy (EDXS), the Opal 410 automatic machine (ATM GmbH, Germany) was used for the preparation of the metallographic samples. Bulk pieces of alloys were carefully positioned on the sample stage, coated first with phenolic resin and then with Bakelite, and hot-pressed at 180 °C. The metallographic samples were cleaned and polished using the Saphir 520 automatic lapping machine (ATM GmbH, Germany). SiC papers with a grain size of 400–1000 mesh were used to clean the sample surface, while thin plates with a grain size of 6–1 μm were used for polishing. Ethanol was used as a solvent throughout the procedure. Samples were analyzed for microstructural features and phase compositions using a Zeiss Evo 40 SEM (Carl Zeiss SMT Ltd, Cambridge, England) supplied by the *Inca Energy* Program. The instrument is coupled with a backscattered electron (BSE) detector and an EDXS. A cobalt standard was used to calibrate the instrument, which was operated with an accelerating voltage of 20 keV, a working distance of 12 mm, and a counting time of 100 s. For the qualitative analysis, the X-ray spectra obtained from the contact of the sample with the electron beam were compared with the spectra of the pure elements from the database. For the quantitative analysis, the ZAF factor was automatically applied to the peak intensities, taking into account the atomic number (Z), absorption (A) and fluorescence (F).

Powder X-ray diffraction (XRD) of the polycrystalline samples was performed using a X'Pert MPD vertical diffractometer (Philips, Almelo, The Netherlands) at a wavelength of $\lambda_{Cu\text{-}K\alpha} = 1.5406$ Å. For this technique, small pieces of alloy were crushed into a fine powder using a mortar and pestle. The powder was then placed in the cavity of a zero-background silicon holder. The obtained powder patterns were indexed using the program POWDERCELL [20] and the lattice parameters (with standard error values) were derived using the software CELREF [21]. The structure refinement of some ternary compounds was performed with the Rietveld method using FULLPROF [22]. The diffraction patterns for these compounds were obtained in the range $18° \leq 2\theta \leq 115°$ (scan step size 0.02 °, step time 45–70 s).

Magnetic susceptibility measurements for selected compositions were carried out in the temperature range of 2–400 K using the PPMS–VSM (Physical Properties Measuring System–Vibrating Sample Magnetometer) from Quantum Design San Diego, USA. Samples weighing 30–35 mg were placed in a thin plastic tube carefully positioned in a sample holder (almost 35 mm from the bottom of the sample holder). The sample holder, secured in a rod, was placed in the VSM by setting it to automatic centering, maintaining a temperature of 300 K and zero applied field.

Table 2
SEM EDXS and XRD characterization results of the Yb–Cu–Zn samples.

N.	Nominal composition of alloy (at%)	Phase analysis	EDXS at% Yb;Cu;Zn	Crystal structure	Lattice parameters (nm)		
					a	*b*	*c*
1	$Yb_{25}Cu_{50}Zn_{25}$	$Yb(Cu,Zn)_2$	34;36;30	Orthorhombic *oI*12-KHg_2	0.4393(1)	0.7069(2)	0.7481(2)
		$YbCu_{4.5-x}Zn_x$ ($x = 1.2$)	18;60;22	Monoclinic $YbCu_{4.5}$			
2	$Yb_{25}Cu_{25}Zn_{50}$	τ_2-$YbCu_{5-x}Zn_x$ ($x = 3.0$)	17;33;50	Hexagonal *hP*6-$CaCu_5$	0.5218(3)		0.4187(1)
		$Yb(Cu,Zn)_2$	34;16;50	Orthorhombic *oI*12-KHg_2	0.4512(2)	0.7198(6)	0.7513(4)
3	$Yb_{19}Cu_{60}Zn_{21}$	$YbCu_{4.5-x}Zn_x$ ($x = 1.3$)	18;59;23	Monoclinic $YbCu_{4.5}$			
4	$Yb_{17}Cu_{34}Zn_{49}$	τ_2-$YbCu_{5-x}Zn_x$ ($x = 3.0$)	17;34;49	Hexagonal *hP*6-$CaCu_5$	0.52150(1)		0.41998(1)
5	$Yb_{28}Cu_{29}Zn_{43}$	$Yb(Cu,Zn)_2$	34;22;44	Orthorhombic *oI*12-KHg_2	0.4481(4)	0.7149(9)	0.7506(7)
		τ_2-$YbCu_{5-x}Zn_x$ ($x = 2.6$)	17;40;43	Hexagonal *hP*6-$CaCu_5$	0.5201(8)		0.4169(1)
6	$Yb_{33}Cu_{17}Zn_{50}$	$Yb(Cu,Zn)_2$	33;17;50	Orthorhombic *oI*12-KHg_2	0.4510(1)	0.7190(1)	0.7497(2)
7	$Yb_{17}Cu_{40}Zn_{43}$	τ_2-$YbCu_{5-x}Zn_x$ ($x = 2.6$)	17;40;43	Hexagonal *hP*6-$CaCu_5$	0.5199(3)		0.41706(4)
8	$Yb_{10}Cu_{60}Zn_{30}$	τ_2-$YbCu_{5-x}Zn_x$ ($x = 1.8$)	17;53;30	Hexagonal *hP*6-$CaCu_5$	0.5130(4)		0.41567(3)
		(Cu)	0;68;32	Cubic *cF*4-Cu	0.3686(1)		
		τ_1-$YbCu_{5-x}Zn_x$ ($x = 1.5$)	17;58;25	Cubic *cF*24-$AuBe_5$			
9	$Yb_{17}Cu_{50}Zn_{33}$	τ_2-$YbCu_{5-x}Zn_x$ ($x = 2.1$)	17;49;34	Hexagonal *hP*6-$CaCu_5$	0.5168(1)		0.41430(3)
		$YbCu_{4.5-x}Zn_x$ ($x = 1.6$)	18;54;28	Monoclinic $YbCu_{4.5}$			
10	$Yb_{17}Cu_{56}Zn_{27}$	τ_2-$YbCu_{5-x}Zn_x$ ($x = 1.8$)	17;53;30	Hexagonal *hP*6-$CaCu_5$	0.5151(3)		0.41379(4)
		τ_1-$YbCu_{5-x}Zn_x$ ($x = 1.5$)	17;58;25	Cubic *cF*24-$AuBe_5$	0.7074(6)		
11	$Yb_{17}Cu_{17}Zn_{66}$	τ_2-$YbCu_{5-x}Zn_x$ ($x = 4.0$)	17;16;67	Hexagonal *hP*6-$CaCu_5$	0.5270(2)		0.42398(4)
12	$Yb_{17}Cu_{70}Zn_{13}$	τ_1-$YbCu_{5-x}Zn_x$ ($x = 0.8$)	17;70;13	Cubic *cF*24-$AuBe_5$	0.7027(5)		
		(Cu)	0;79;21	Cubic *cF*4-Cu			
13	$Yb_{17}Cu_{68}Zn_{15}$	τ_1-$YbCu_{5-x}Zn_x$ ($x = 0.9$)	17;68;15	Cubic *cF*24-$AuBe_5$	0.7034(6)		
		(Cu)	0;78;22	Cubic *cF*4-Cu			
14	$Yb_{17}Cu_{66}Zn_{17}$	τ_1-$YbCu_{5-x}Zn_x$ ($x = 1.0$)	17;66;17	Cubic *cF*24- $AuBe_5$	0.70399(2)		
		(Cu)	0;77;23	Cubic *cF*4-Cu			
15	$Yb_{33}Cu_{50}Zn_{17}$	$Yb(Cu,Zn)_2$	34;48;18	Orthorhombic *oI*12-KHg_2	0.4346(2)	0.6993(4)	0.7444(3)
		$YbCu_{4.5-x}Zn_x$ ($x = 1.0$)	18;64;18	Monoclinic $YbCu_{4.5}$			
16	$Yb_{17}Cu_{63}Zn_{20}$	τ_1-$YbCu_{5-x}Zn_x$ ($x = 1.3$)	17;62;21	Cubic *cF*24-$AuBe_5$	0.7054(2)		
		$YbCu_{4.5-x}Zn_x$ ($x = 1.1$)	18;62;20	Monoclinic $YbCu_{4.5}$			
17	$Yb_{18}Cu_{62}Zn_{20}$	$YbCu_{4.5-x}Zn_x$ ($x = 1.1$)	18;62;20	Monoclinic $YbCu_{4.5}$			
18	$Yb_{17}Cu_{13}Zn_{70}$	τ_2-$YbCu_{5-x}Zn_x$ ($x = 4.2$)	17;13;70	Hexagonal *hP*6-$CaCu_5$	0.5291(3)		0.42414(4)
		τ_3-Yb_2CuZn_7	20;8;72	Unknown			
19	$Yb_{33}Cu_{29}Zn_{38}$	$Yb(Cu,Zn)_2$	33;28;39	Orthorhombic *oI*12-KHg_2	0.4447(2)	0.7110(3)	0.7480(3)
		$YbCu_{4.5-x}Zn_x$ ($x = 1.7$)	20;50;30	Monoclinic $YbCu_{4.5}$			
20	$Yb_{60}Cu_{16}Zn_{24}$	τ_4-$Yb_5Cu_{2-x}Zn_{1+x}$ ($x = 0.7$)	62;17;21	Tetragonal *tI*32-Mo_5B_2Si	0.7792(2)		1.45608(4)
		$YbZn_{1-x}Cu_x$ ($x = 0.24$)	50;12;38	Cubic *cP*2-CsCl	0.3611(2)		
21	$Yb_{17}Cu_8Zn_{75}$	$Yb_{13}Cu_xZn_{58-x}$ ($x = 3.5$)	18;5;75	Hexagonal *hP*142-$Gd_{13}Zn_{58}$			
		τ_2-$YbCu_{5-x}Zn_x$ ($x = 4.4$)	17;9;74	Hexagonal *hP*6-$CaCu_5$	0.5300(3)		0.4248(1)

(*continued on next page*)

Table 2 (*continued*)

N.	Nominal composition of alloy (at%)	Phase analysis	EDXS at% Yb;Cu;Zn	Crystal structure	Lattice parameters (nm)		
					a	*b*	*c*
22	$Yb_{22}Cu_{60}Zn_{18}$	$YbCu_{4.5-x}Zn_x$ ($x = 1.0$)	20;62;18	Monoclinic $YbCu_{4.5}$			
		$Yb(Cu,Zn)_2$	33;47;20	Orthorhombic *oI*12-KHg_2			
23	[a]$Yb_{50}Cu_{12}Zn_{38}$	$YbZn_{1-x}Cu_x$ ($x = 0.14$)	50;8;42	Cubic *cP*2-CsCl	0.3613(1)		
		$Yb(Cu,Zn)_2$	35;30;35	Orthorhombic *oI*12-KHg_2			
		τ_4-$Yb_5Cu_{2-x}Zn_{1+x}$ ($x = 0.7$)	62;17;21	Tetragonal *tI*32-Mo_5B_2Si			
24	$Yb_{63}Cu_7Zn_{30}$	τ_4-$Yb_5Cu_{2-x}Zn_{1+x}$ ($x = 1.2$)	63;10;27	Tetragonal *tI*32-Mo_5B_2Si	0.7848(5)		1.4711(2)
		$YbZn_{1-x}Cu_x$ ($x = 0.05$)	50;2;48	Cubic *cP*2-CsCl	0.3621(3)		
		(Yb)	98;0;2	Cubic *cF*4-Cu			
25	$Yb_{63}Cu_{30}Zn_7$	τ_4-$Yb_5Cu_{2-x}Zn_{1+x}$ ($x = -0.3$)	63;28;9	Tetragonal *tI*32-Mo_5B_2Si	0.7703(6)		1.4501(1)
		$YbCu_{1-x}Zn_x$ ($x = 0.1$)	50;45;5	Orthorhombic *oP*8-FeB			
		(Yb)	98;2;0	Cubic *cF*4-Cu			
26	$Yb_{24}Cu_8Zn_{68}$	τ_3-Yb_2CuZn_7	20;10;70	Unknown			
		$Yb(Cu,Zn)_2$	33;2;65	Orthorhombic *oI*12-KHg_2	0.4554(4)	0.7277(5)	0.7547(8)
27	$Yb_{20}Cu_{10}Zn_{70}$	τ_3-Yb_2CuZn_7	20;10;70	Unknown			
		τ_2-$YbCu_{5-x}Zn_x$ ($x = 4.1$)	17;15;68	Hexagonal *hP*6-$CaCu_5$			
28	$Yb_{33}Cu_{10}Zn_{57}$	$Yb(Cu,Zn)_2$	34;9;57	Orthorhombic *oI*12-KHg_2	0.4532(2)	0.7232(2)	0.7508(4)
		τ_2-$YbCu_{5-x}Zn_x$ ($x = 3.2$)	17;29;54	Hexagonal *hP*6-$CaCu_5$			
29	$Yb_{33}Cu_{60}Zn_7$	$Yb(Cu,Zn)_2$	34;58;8	Orthorhombic *oI*12-KHg_2	0.4310(2)	0.6927(3)	0.7401(3)
		$YbCu_{4.5-x}Zn_x$ ($x = 0.5$)	20;70;10	Monoclinic $YbCu_{4.5}$			
30	$Yb_{20}Cu_{50}Zn_{30}$	$YbCu_{4.5-x}Zn_x$ ($x = 1.7$)	19;51;30	Monoclinic $YbCu_{4.5}$			
		$Yb(Cu,Zn)_2$	33;28;39	Orthorhombic *oI*12-KHg_2			
31	$Yb_{50}Cu_{30}Zn_{20}$	$YbCu_{1-x}Zn_x$ ($x = 0.35$)	50;32;18	Orthorhombic *oP*8-FeB	0.7693(4)	0.4307(1)	0.5851(2)
		$Yb(Cu,Zn)_2$	33;31;36	Orthorhombic *oI*12-KHg_2			
		τ_4-$Yb_5Cu_{2-x}Zn_{1+x}$ ($x = 0.4$)	63;19;18	Tetragonal *tI*32-Mo_5B_2Si			
32	$Yb_{76}Cu_5Zn_{19}$	τ_4-$Yb_5Cu_{2-x}Zn_{1+x}$ ($x = 1.2$)	63;10;27	Tetragonal *tI*32-Mo_5B_2Si	0.7867(9)		1.4729(2)
		(Yb)	98;0;2	Cubic *cF*4-Cu	0.5480(3)		
33	$Yb_{57}Cu_{14}Zn_{29}$	τ_4-$Yb_5Cu_{2-x}Zn_{1+x}$ ($x = 0.4$)	63;19;18	Tetragonal *tI*32-Mo_5B_2Si	0.7795(2)		1.45513(3)
		$YbZn_{1-x}Cu_x$ ($x = 0.1$)	50;5;45	Cubic *cP*2-CsCl	0.36141(5)		
34	[a]$Yb_{50}Cu_{21}Zn_{29}$	$YbZn_{1-x}Cu_x$ ($x = 0.4$)	50;20;30	Cubic *cP*2-CsCl	0.3612(1)		
		$YbCu_{1-x}Zn_x$		Orthorhombic *oP*8-FeB	7.686(6)	4.306(1)	5.849(3)
		τ_4-$Yb_5Cu_{2-x}Zn_{1+x}$ ($x = 0.4$)	63;19;18	Tetragonal *tI*32-Mo_5B_2Si			
		$Yb(Cu,Zn)_2$	35;28;37	Orthorhombic *oI*12-KHg_2			
35	$Yb_{18}Cu_{48}Zn_{34}$	$YbCu_{4.5-x}Zn_x$ ($x = 1.7$)	19;50;31	Monoclinic $YbCu_{4.5}$			
		τ_2-$YbCu_{5-x}Zn_x$ ($x = 2.3$)	17;44;39	Hexagonal *hP*6-$CaCu_5$	0.5181(1)		0.41537(2)
36	$Yb_{33}Cu_{42}Zn_{25}$	$Yb(Cu,Zn)_2$	34;40;26	Orthorhombic *oI*12-KHg_2	0.4367(2)	0.7037(4)	0.7475(4)
		$YbCu_{4.5-x}Zn_x$ ($x = 1.3$)	20;57;23	Monoclinic $YbCu_{4.5}$			
37	$Yb_{21}Cu_3Zn_{76}$	$Yb_3Zn_{11-x}Cu_x$ ($x = 0.5$)	22;3;75	Orthorhombic *oI*28-La_3Al_{11}	0.4407(2)	0.8842(7)	1.3098(6)
		$Yb_{13}Zn_{58-x}Cu_x$ ($x = 3.0$)	18;4;78	Hexagonal *hP*142-$Gd_{13}Zn_{58}$	1.4233(4)		1.41431(3)

(*continued on next page*)

Table 2 (*continued*)

N.	Nominal composition of alloy (at%)	Phase analysis	EDXS at% Yb;Cu;Zn	Crystal structure	Lattice parameters (nm)		
					a	*b*	*c*
38	$Yb_{18}Cu_3Zn_{79}$	$Yb_{13}Zn_{58-x}Cu_x$ ($x = 2.2$)	18;3;79	Hexagonal *hP*142-$Gd_{13}Zn_{58}$	1.4265(8)		1.4084(1)
		$Yb_3Zn_{17-x}Cu_x$ ($x = 1.0$)	16;5;79	Cubic *cI*160-$Be_{17}Ru_3$			
39	$Yb_{15}Cu_3Zn_{82}$	$Yb_3Zn_{17-x}Cu_x$ ($x = 0.6$)	16;3;81	Cubic *cI*160-$Be_{17}Ru_3$	1.4230(4)		
		$Yb_2Zn_{17-x}Cu_x$ ($x = 1.2$)	11;6;83	Hexagonal *hR*57-Th_2Zn_{17}			
40	$Yb_6Cu_{57}Zn_{37}$	$Yb_2Zn_{17-x}Cu_x$ ($x = 9.5$)	11;50;39	Hexagonal *hR*57-Th_2Zn_{17}	0.8759(3)		1.2724(2)
		(Cu)	0;66;34	Cubic *cF*4-Cu	0.3688(6)		
41	$Yb_6Cu_{42}Zn_{52}$	$Yb_2Zn_{17-x}Cu_x$ ($x = 6.5$)	11;34;55	Hexagonal *hR*57-Th_2Zn_{17}	0.8832(5)		1.2816(3)
		β	0;51;49	Cubic *cP*2-CsCl	0.2954(6)		
42	$Yb_6Cu_{24}Zn_{70}$	$YbZn_{11-x}Cu_x$ ($x = 2.2$)	8;18;74	Tetragonal *tI*48-$BaCd_{11}$	1.0511(6)		0.67664(7)
		γ	0;38;62	Cubic *cI*52-Cu_5Zn_8	0.8862(4)		
		$Yb_2Zn_{17-x}Cu_x$ ($x = 3.8$)	11;20;69	Hexagonal *hR*57-Th_2Zn_{17}			
43	$Yb_6Cu_{14}Zn_{80}$	$YbZn_{11-x}Cu_x$ ($x = 1.1$)	8;9;83	Tetragonal *tI*48-$BaCd_{11}$	1.0593(8)		0.67683(7)
		δ	0;23;77	Hexagonal *hP*2-Mg	0.2734(2)		0.42882(9)
		γ	0;33;67	Cubic *cI*52-Cu_5Zn_8			
44	$Yb_{11}Cu_{20}Zn_{69}$	$Yb_2Zn_{17-x}Cu_x$ ($x = 3.6$)	11;19;70	Hexagonal *hR*57-Th_2Zn_{17}	0.8887(9)		1.2908(5)
		τ_2-$YbCu_{5-x}Zn_x$ ($x = 4.0$)	17;16;67	Hexagonal *hP*6-$CaCu_5$			
45	$Yb_{11}Cu_{54}Zn_{35}$	$Yb_2Zn_{17-x}Cu_x$ ($x = 10.1$)	11;53;36	Hexagonal *hR*57-Th_2Zn_{17}	0.8762(4)		1.2718(2)
		τ_2-$YbCu_{5-x}Zn_x$ ($x = 1.9$)	16;52;32	Hexagonal *hP*6-$CaCu_5$			
		(Cu)	0;67;33	Cubic *cF*4-Cu			
46	$YbCu_2Zn_{20}$	$YbZn_{11-x}Cu_x$ ($x = 0.8$)	9;7;84	Tetragonal *tI*48-$BaCd_{11}$	1.059(3)		0.6764(2)
		L	0;14;86	Hexagonal *hP*2-Mg			
47	$Yb_{11}Cu_{69}Zn_{20}$	τ_1-$YbCu_{5-x}Zn_x$ ($x = 1.1$)	17;65;18	Cubic *cF*24- $AuBe_5$	0.7041(3)		
		(Cu)	0;76;24	Cubic *cF*4-Cu	0.3673(4)		
48	$Yb_{11}Cu_{79}Zn_{10}$	τ_1-$YbCu_{5-x}Zn_x$ ($x = 0.5$)	17;75;8	Cubic *cF*24- $AuBe_5$	0.6996(4)		
		(Cu)	0;86;14	Cubic *cF*4-Cu	0.3644(2)		
49	[a]$Yb_{17}Cu_{72}Zn_{11}$	τ_1-$YbCu_{5-x}Zn_x$ ($x = 0.7$)	17;71;12	Cubic *cF*24-$AuBe_5$	0.7022(4)		
		$YbCu_{4.5-x}Zn_x$ ($x = 0.6$)	18;71;11	Monoclinic $YbCu_{4.5}$			
		(Cu)	0;81;19	Cubic *cF*4-Cu			
50	[a]$Yb_{17}Cu_{73}Zn_{10}$	τ_1-$YbCu_{5-x}Zn_x$ ($x = 0.6$)	17;72;11	Cubic *cF*24-$AuBe_5$	0.7012(9)		
		$YbCu_{4.5-x}Zn_x$ ($x = 0.5$)	18;73;9	Monoclinic $YbCu_{4.5}$			
		(Cu)	0;82;18	Cubic *cF*4-Cu			
51	[a]$Yb_{17}Cu_{75}Zn_8$	τ_1-$YbCu_{5-x}Zn_x$ ($x = 0.5$)	17;74;9	Cubic *cF*24-$AuBe_5$	0.7008(3)		
		$YbCu_{4.5-x}Zn_x$ ($x = 0.5$)	18;74;8	Monoclinic $YbCu_{4.5}$			
		(Cu)	0;84;16	Cubic *cF*4-Cu			
52	[a]$Yb_{17}Cu_{77}Zn_6$	τ_1-$YbCu_{5-x}Zn_x$ ($x = 0.4$)	17;75;8	Cubic *cF*24-$AuBe_5$	0.7003(5)		
		$YbCu_{4.5-x}Zn_x$ ($x = 0.4$)	18;76;6	Monoclinic $YbCu_{4.5}$			
		(Cu)	0;86;14	Cubic *cF*4-Cu			

(*continued on next page*)

Table 2 (*continued*)

N.	Nominal composition of alloy (at%)	Phase analysis	EDXS at% Yb;Cu;Zn*	Crystal structure	Lattice parameters (nm)		
					a	*b*	*c*
53	$Yb_{17}Cu_{78}Zn_5$	$YbCu_{4.5-x}Zn_x$ ($x = 0.3$)	18;78;4	Monoclinic $YbCu_{4.5}$			
		(Cu)	0;88;12	Cubic *cF*4-Cu			

* Compositions measured by EDXS with an accuracy of ~ 1 at%.
[a] Sample not in equilibrium

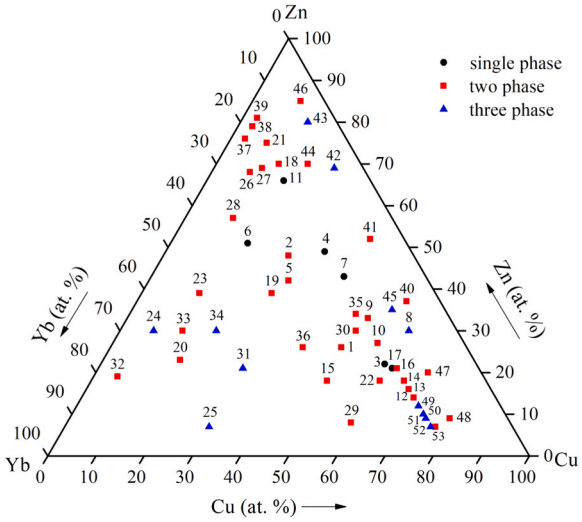

Fig. 1. EDXS compositions of selected samples prepared in the Yb–Cu–Zn system.

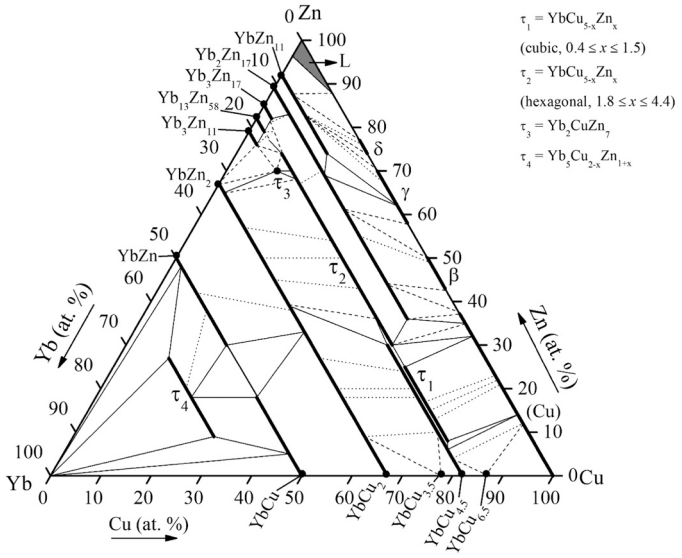

Fig. 2. Phase equilibria at 600 °C of samples prepared in the Yb–Cu–Zn system. Thick lines represent solid solutions, thin lines delimitate three-phase regions, dot-lines represent some determined tie-lines, dashed-lines are tentative equilibria.

4. Results and discussion

Fifty-three samples were prepared and analyzed in the Yb–Cu–Zn system. The experimental results of the EDXS and XRD analysis of the phases are listed in Table 2 for several alloys, while Fig. 1 shows the EDXS compositions of these samples on the Gibbs triangle. These compositions were always very close to the nominal compositions of the samples. The *x* concentration of the third element, i.e copper or zinc, is calculated from the corresponding EDXS data.

The Yb–Cu–Zn isothermal section obtained over the entire concentration range at 600 °C is shown in Fig. 2. At this temperature, the Zn-rich region of the phase diagram is characterized by the presence of a liquid phase. The region where the liquid and solid phases coexist is indicated by a dashed line. The crystallographic data of the ternary phases can be found in Table 3.

A striking feature of this phase diagram is the presence of extensive substitutional Cu/Zn solid solutions forming in the ternary region or originating from the Yb–Cu and Yb–Zn binary systems. Such homogeneity regions were also found in the isothermal section of Ce–Cu–Zn investigated by Pavlyuk *et al.* [23]. However, in the case of the Yb–Cu–Zn ternary system, striking differences were observed, as we will see in the next sections.

The Yb-Cu-Zn system is characterized by the existence of four ternary compounds, namely τ_1: $YbCu_{5-x}Zn_x$ (cubic $AuBe_5$ type, $0.4 < x \leq 1.5$), τ_2: $YbCu_{5-x}Zn_x$ (hexagonal $CaCu_5$ type, $1.8 \leq x \leq 4.4$), τ_3-Yb_2CuZn_7 and τ_4: $Yb_5Cu_{2-x}Zn_{1+x}$ (tetragonal Mo_5B_2Si type, 9–28 at% Zn in Cu). In addition, further phases are formed from several binary compounds, namely the solid solution $Yb(Cu,Zn)_2$, which forms continuously from the isotypic compounds $YbCu_2$ and $YbZn_2$, and the extended Cu/Zn substitutional degrees in YbZn (up to 20 at% Cu in Zn), YbCu (up to 18 at% Zn in Cu), $YbCu_{4.5}$ (up to 30 at% Zn in Cu), Yb_2Zn_{17} and $YbZn_{11}$ (the solubility of Cu in Zn is up to 54 and 18 at%, respectively).

While the $Ce(Cu,Zn)_5$ solid solution originating from the pseudobinary $CeCu_5$-$CeZn_5$ system crystallizes only in the hexagonal $CaCu_5$ prototype [24], interestingly, two crystal structures are formed at the $YbCu_{5-x}Zn_x$ composition line, which are stabilized by different amounts of Zn. Starting from low Zn values, the cubic $AuBe_5$ phase (sp. gr. $F\bar{4}3m$) stabilizes at a concentration of $0.4 \leq x \leq 1.5$, while a further increase in concentration in the range of $1.8 \leq x \leq 4.4$ leads to a hexagonal $CaCu_5$-type structure (sp. gr. *P6/mmm*).

Fig. 3 shows the trend of the lattice parameter values for the $YbCu_{5-x}Zn_x$ series plotted against the *x* concentration of Zn. The increasing trend of the lattice parameters for both structures is consistent with the larger size of the Zn atoms compared to the Cu atoms. Furthermore, the values are in good agreement with Vegard's law, as shown by the linear fit. The values of the lattice parameters shown in Fig. 3b are compared with those of $YbCu_{6.5}$, since the latter exists under equilibrium conditions instead of $YbCu_5$ [12].

Another phase that competes with the cubic phase is found at Zn contents of less than 30 at%, where the cubic phase is stable. As in the case of $YbCu_{5-x}Au_x$ [12], a $YbCu_{4.5-x}Zn_x$ phase formed from $YbCu_{4.5}$ (a

Table 3
Ternary phases determined in the Yb–Cu–Zn system.

Phase	Pearson symbol/prototype	Lattice parameters (nm)		Alloy N. [Ref.]
		a	*c*	
τ_1-$YbCu_{5-x}Zn_x$	Cubic *cF*24-$AuBe_5$			
$x = 1.5$		0.7074(6)		**8** [This work]
$x = 1.3$		0.7054(2)		**16** [This work]
$x = 1.1$		0.7041(3)		**47** [This work]
$x = 1.0$		0.7046		[9]
$x = 1.0$		0.70399(2)		**14** [This work]
$x = 0.9$		0.7034(6)		**13** [This work]
$x = 0.8$		0.7027(5)		**12** [This work]
$x = 0.7$		0.7022(4)		**49** [This work]
$x = 0.6$		0.7012(9)		**50** [This work]
$x = 0.5$		0.6996(4)		**48** [This work]
$x = 0.5$		0.7008(3)		**51** [This work]
$x = 0.4$		0.7003(5)		**52** [This work]
τ_2-$YbCu_{5-x}Zn_x$	Hexagonal *hP*6-$CaCu_5$			
$x = 4.4$		0.5300(3)	0.4248(1)	**21** [This work]
$x = 4.2$		0.5291(3)	0.42414(4)	**18** [This work]
$x = 4.0$		0.5270(2)	0.42398(4)	**11** [This work]
$x = 3.0$		0.5218(3)	0.4187(1)	**2** [This work]
$x = 3.0$		0.52150(1)	0.41998(1)	**4** [This work]
$x = 2.6$		0.5201(8)	0.4169(1)	**5** [This work]
$x = 2.6$		0.5199(3)	0.41706(4)	**7** [This work]
$x = 2.3$		0.5181(1)	0.41537(2)	**35** [This work]
$x = 2.1$		0.5168(1)	0.41430(3)	**9** [This work]
$x = 1.8$		0.5130(4)	0.41567(3)	**8** [This work]
$x = 1.8$		0.5151(3)	0.41379(4)	**10** [This work]
τ_3-Yb_2CuZn_7	Unknown			**18, 26, 27** [This work]
τ_4-$Yb_5Cu_{2-x}Zn_{1+x}$	Tetragonal *tI*32 Mo_5B_2Si			
$x = 1.2$		0.7848(5)	1.4711(2)	**24** [This work]
$x = 1.2$		0.7867(9)	1.4729(2)	**32** [This work]
$x = 0.7$		0.7792(2)	1.45608(4)	**20** [This work]
$x = 0.4$		0.7795(2)	1.45513(3)	**33** [This work]
$x = 0.0$		0.7766(1)	1.4533(2)	[19]
$x = -0.3$		0.7703(6)	1.4501(1)	**25** [This work]

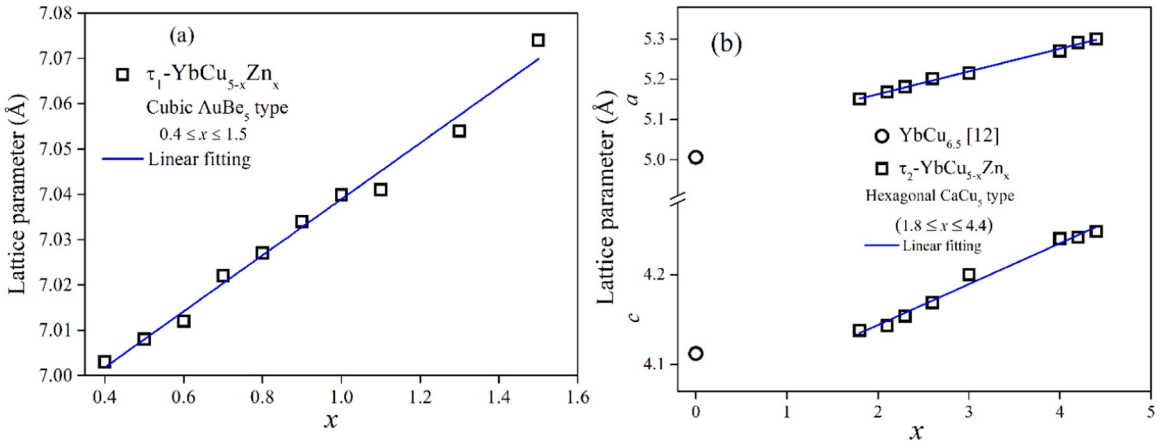

Fig. 3. Unit cell parameters plotted against Zn x concentration for (a) cubic τ_1-$YbCu_{5-x}Zn_x$ compositions ($0.4 \leq x \leq 1.5$) and (b) hexagonal τ_2-$YbCu_{5-x}Zn_x$ compositions ($1.8 \leq x \leq 4.4$); blue lines indicate linear fitting.

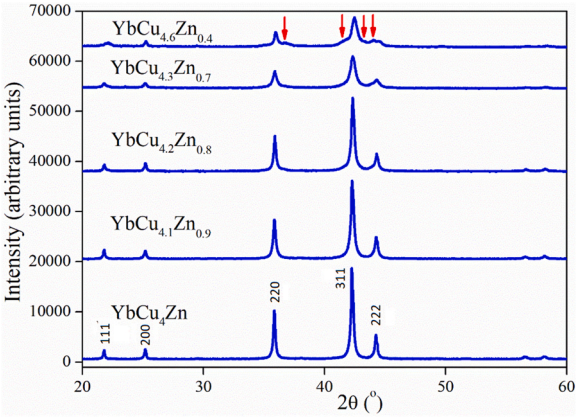

Fig. 4. X-ray diffraction (CuK_α) powder patterns for selected τ_1-$YbCu_{5-x}Zn_x$ compositions. The red arrows indicate the peaks of the $YbCu_{4.5}$-type superstructure.

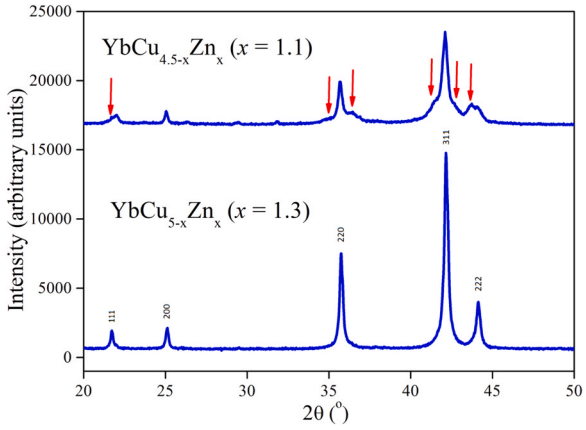

Fig. 5. XRD comparison between samples N. 16 and N.17. The red arrows indicate the peaks of the $YbCu_{4.5}$-type superstructure.

very complex monoclinic superstructure of the cubic $AuBe_5$-phase) is stable to the lower limit of solubility of the hexagonal phase according to the XRD powder patterns.

Fig. 4 shows a comparison of the XRD measurements of $YbCu_{5-x}Zn_x$ compositions. The difference between the cubic $AuBe_5$ and the monoclinic superstructure is very subtle. While the XRD patterns of the samples in the range $0.7 < x < 1.0$ were fully indexed with the cubic $AuBe_5$ type, the Bragg peaks in the pattern of the sample at $x = 0.4$ show a general broadening and, additionally, the presence of some satellite peaks around the main peaks, similar to the pattern of $YbCu_{4.5}$ [12]. The samples in the range $0.4 \leq x < 0.7$, which correspond to samples N.49–52 in Table 2, show the coexistence of the cubic phase with its superstructure along the $YbCu_{5-x}Zn_x$ line with varying composition of the two phases and are probably not in equilibrium.

The two compounds τ_1-$YbCu_{5-x}Zn_x$ and $YbCu_{4.5-x}Zn_x$ are very close in composition: they both extend parallel to each other, with the Cu/Zn substitution occurring at a distance of only 1.5 at% Yb. Fig. 5 shows the formation of the $YbCu_{4.5}$ superstructure in the XRD pattern of sample N. 17 ($Yb_{18}Cu_{62}Zn_{20}$), which is very close in composition to sample N. 16 ($Yb_{17}Cu_{63}Zn_{20}$), which is indexed as a cubic $AuBe_5$- type.

Fig. 6a shows the BSE image of sample N. 52, which represents the region of equilibrium of the three phases τ_1-$YbCu_{5-x}Zn_x$, $YbCu_{4.5-x}Zn_x$ and (Cu).

A composition along τ_1-$YbCu_{5-x}Zn_x$ ($YbCu_4Zn$, $x = 1.0$) was synthesized by Sarrao *et al.* [9] to study its physical properties. $YbCu_4Zn$ was synthesized in this work and identified in sample N. 14 (see Fig. 7). The structural refinement of the compound was performed using the disordered prototype $AuBe_5$ instead of the ternary ordered variant $MgCu_4Sn$. Due to the similar X-ray scattering factors and atomic radii of the Cu and Zn atoms, we cannot identify the Cu/Zn ordering at sites 16e and 4c. Therefore, the occupancies of these two atoms at these sites were set to 50%. The atomic coordinates are shown in Table 4.

The XRD and SEM analyzes of sample N. 4, which belongs to τ_2-$YbCu_{5-x}Zn_x$ ($x = 3.0$), are shown in Fig. 8. The sample is single-phase and its powder XRD pattern was successfully indexed with the hexagonal $CaCu_5$ prototype (sp. gr. *P6/mmm*). For the reasons explained above, the refinement of the atomic sites was performed by fixing the occupation of Cu and Zn atoms at 50%. The refinement leads to good values for the reliability factors ($R_B = 5.48$, $R_f = 5.00$). The refined atomic coordinates are shown in Table 5. Fig. 6b shows the BSE image of the sample N. 8, in which the two compounds τ_1-$YbCu_{5-x}Zn_x$ and τ_2-$YbCu_{5-x}Zn_x$ can hardly be distinguished due to the low compositional contrast.

A new ternary compound with a composition of 20 at% Yb, 8–10 at% Cu, and 72–70 at% Zn was detected in samples N. 18, N. 26 and 27 (see Fig. 9a). All attempts to index the XRD patterns or to obtain single crystals from bulk pieces were unsuccessful. A tentative formula τ_3-Yb_2CuZn_7 was obtained from the EDXS composition. The crystal structure of the compound is still unknown, and a broader solubility range for this compound cannot be ruled out analogous to the other ternary compounds.

In our work, the already known ternary compound Yb_5Cu_2Zn with a

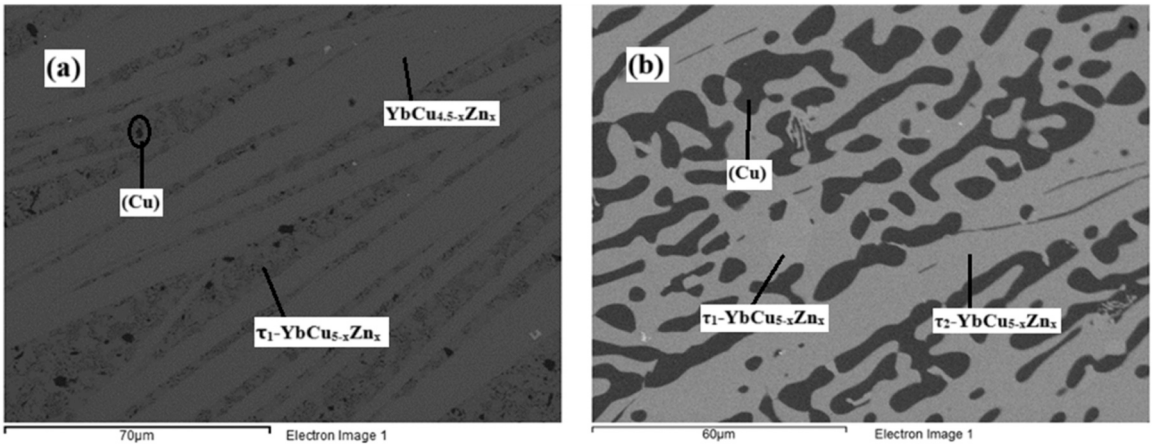

Fig. 6. BSE images of samples illustrating three phases (a) N. 52: matrix (light gray): $YbCu_{4.5-x}Zn_x$ (x = 0.4), dark gray: τ_1-$YbCu_{5-x}Zn_x$ (x = 0.4), and black: (Cu); and (b) N. 8. matrix (gray): τ_2-$YbCu_{5-x}Zn_x$ (x = 1.8), light-gray: τ_1-$YbCu_{5-x}Zn_x$ (x = 1.5) and black: (Cu).

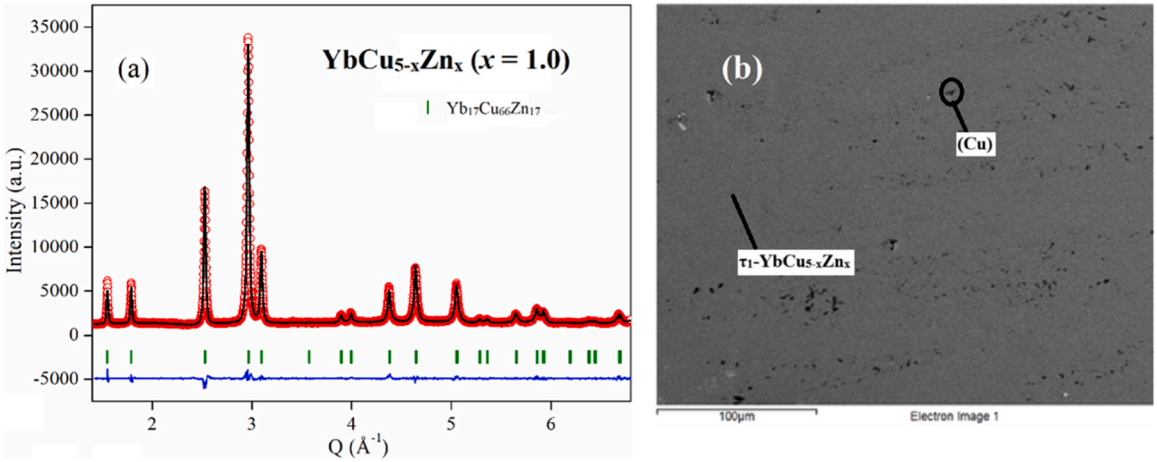

Fig. 7. (a) Rietveld refinement plot for sample N. 14 and (b) BSE image containing: matrix (τ_1-$YbCu_{5-x}Zn_x$, x = 1.0), black crystals (Cu).

Table 4
Standardized atomic coordinates for $YbCu_4Zn$.

Atom	*Site*	x/a	y/b	z/c
Yb	*4a*	0	0	0
M	*16e*	0.62330	0.62330	0.62330
M	*4c*	1/4	1/4	1/4

M = 0.8 Cu + 0.2 Zn (fixed values)

Table 5
Standardized atomic coordinates, refined isotropic thermal factor and occupancies for τ_2-$YbCu_{5-x}Zn_x$, x = 3.0.

Atom	*Site*	x/a	y/b	z/c	B (iso)
Yb	*1a*	0	0	0	0.758(5)
M	*2c*	1/3	2/3	0	1.177(6)
M	*3 g*	1/2	0	1/2	1.180(5)

M = *1/3* Cu + *2/3* Zn (fixed values)

solubility range with the formula: τ_4-$Yb_5Cu_{2-x}Zn_{1+x}$ (concentration range $-0.3 \leq x \leq 1.2$) is formed. The samples prepared along this compound crystallize in the tetragonal structure of Mo_5B_2Si type (sp. gr. *I4/mcm*). The microstructures of samples N. 31, N. 24 and N.25, containing the τ_4-$Yb_5Cu_{2-x}Zn_{1+x}$ compound, are shown in Fig. 9b, Fig. 10a and Fig. 10b, respectively.

The solid solution $Yb(Cu,Zn)_2$ represents the pseudobinary system $YbCu_2$-$YbZn_2$. All samples along this solid solution crystallize in the orthorhombic KHg_2 prototype (sp. gr. *Imma*). Fig. 11 shows a linear increase of the lattice parameter values with increasing *x* concentration (Vegard's law). The microstructure of sample N. 19 is shown in Fig. 12. It contains predominantly the $Yb(Cu,Zn)_2$ phase with 28 at% Cu and traces of the $YbCu_{4.5-x}Zn_x$ phase ($x = 1.7$). The compound YbCuZn [18], known from the literature, is only a composition in the middle of this solid solution.

Two phase branches, which are separated by a two-phase region, form from the binary compounds YbCu and YbZn and both extend into the ternary field. Starting from YbCu, the $YbCu_{1-x}Zn_x$ phase stabilizes up to the concentration of Zn at $x = 0.35$. The samples prepared along the YbCu branch crystallize in the orthorhombic FeB-type structure (sp. gr. *Pnma*). On the other hand, starting from YbZn which crystallizes in the cubic CsCl type structure (sp. gr. $Pm\bar{3}m$), a $YbZn_{1-x}Cu_x$ phase forms up to $x = 0.4$. The microstructure of sample N. 23, which contains $YbZn_{1-x}Cu_x$ ($x = 0.14$) as the majority phase, is shown in Fig. 13. The solid solution $Yb(Cu,Zn)_2$ was detected as a secondary phase.

The maximum solubility of Cu in Yb_2Zn_{17} is 54 at%. The samples prepared along this phase crystallize in the hexagonal Th_2Zn_{17} prototype (sp. gr. $R\bar{3}m$), and the unit cell parameters follow a linear trend with Zn/Cu substitution (Vegard's law), as shown in Fig. 14. The refined XRD powder pattern and the microstructure of the sample N. 44 ($Yb_{11}Cu_{20}Zn_{69}$) prepared along this compound are shown in Fig. 15. The

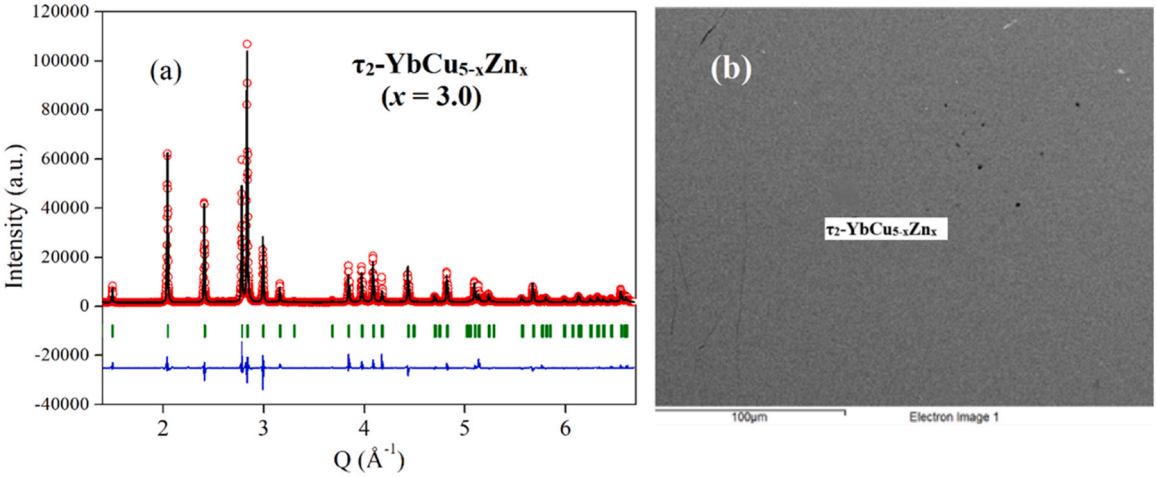

Fig. 8. (a) Rietveld refinement plot for sample N. 4 and (b) BSE image containing single phase τ_2-$YbCu_{5-x}Zn_x$, x = 3.0.

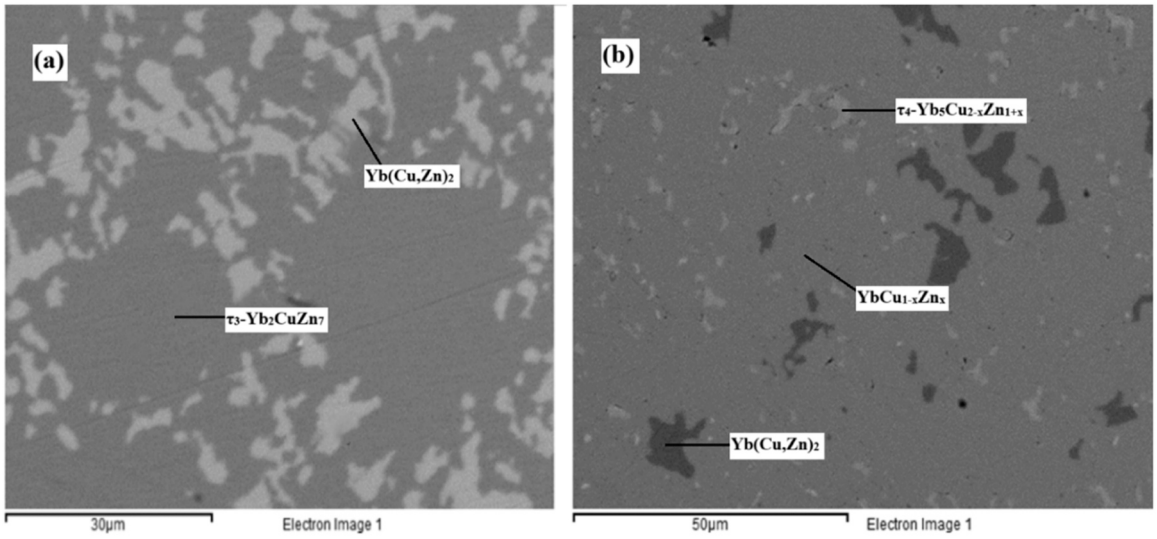

Fig. 9. BSE images of samples (a) N. 26 containing matrix (light-gray): τ_3-Yb_2CuZn_7 and white phase: $Yb(Cu,Zn)_2$ with 2 at% Cu and (b) N. 31. Matrix (light-gray): $YbCu_{1-x}Zn_x$ (x = 0.35), black phase: $Yb(Cu,Zn)_2$ with 31 at% Cu, and white phase: τ_4-$Yb_5Cu_{2-x}Zn_{1+x}$ (x = 0.4).

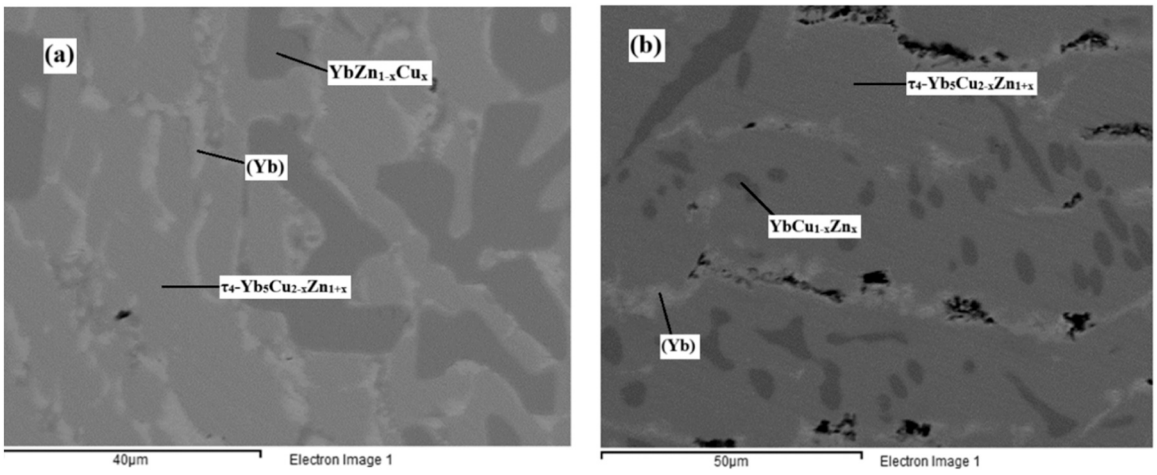

Fig. 10. BSE image of three-phase samples (a) N. 24 containing matrix (light-gray): τ_4-$Yb_5Cu_{2-x}Zn_{1+x}$ (x = 1.2), dark gray phase: $YbZn_{1-x}Cu_x$ (x = 0.05) and white phase: (Yb); and (b) N.25 containing matrix (light-gray): τ_4-$Yb_5Cu_{2-x}Zn_{1+x}$ (x = −0.28), dark gray: $YbCu_{1-x}Zn_x$ (x = 0.1) and white: (Yb).

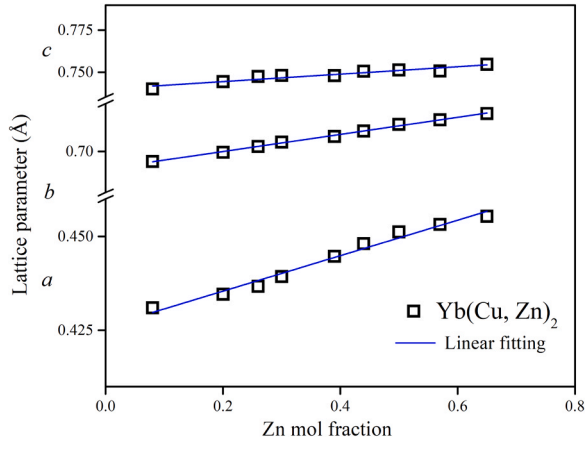

Fig. 11. Lattice parameter trend of $Yb(Cu,Zn)_2$ solid solution plotted against Zn mol fraction. Blue lines indicate linear fitting.

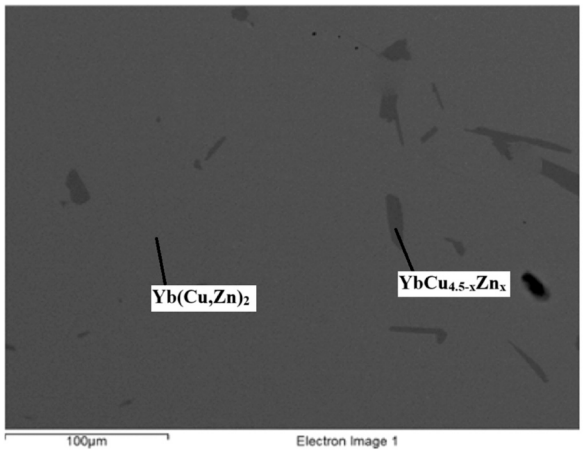

Fig. 12. BSE image of sample N. 19 containing matrix (light-gray): $Yb(Cu,Zn)_2$ (Cu = 28 at%) and dark gray phase: $YbCu_{4.5-x}Zn_x$ (x = 1.7).

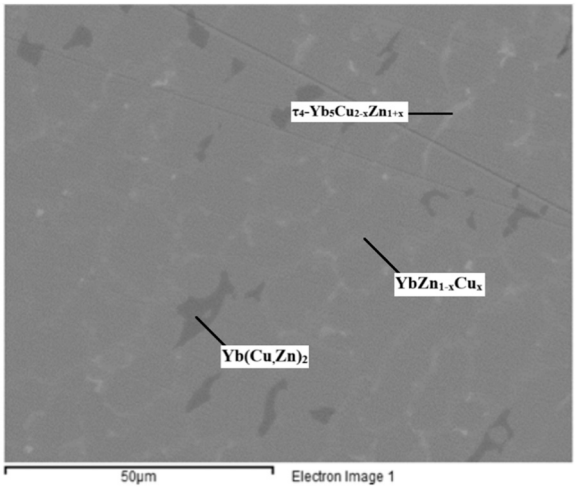

Fig. 13. BSE image of sample N. 23 containing three phases; matrix (light-gray): $YbZn_{1-x}Cu_x$ (x = 0.14), dark gray phase: $Yb(Cu,Zn)_2$ (Cu = 30 at%), and white phase: τ_4-$Yb_5Cu_{2-x}Zn_{1+x}$ (x = 0.7).

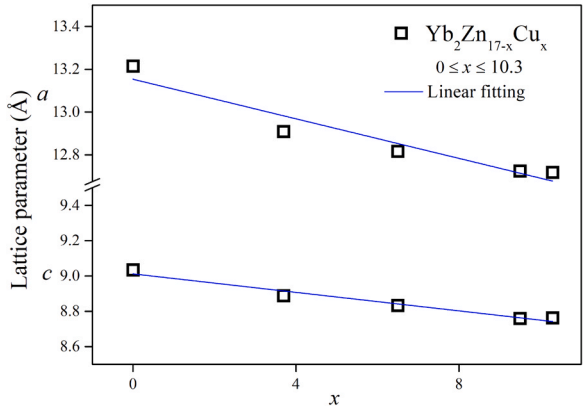

Fig. 14. Lattice parameter trend of $Yb_2Zn_{17-x}Cu_x$ solid solution ($0 \leq x \leq 10.3$) plotted against x.

two phases present are $Yb_2Zn_{17-x}Cu_x$ ($x = 3.6$) together with a small amount of τ_2-$YbCu_{5-x}Zn_x$ ($x = 4.0$). The refinement was performed using the Th_2Zn_{17} model and good reliability factors were obtained ($\chi^2 = 5.20$, $R_B = 5.86$, $R_f = 4.31$).

Fig. 16 shows backscattered electron images of the two samples N. 42 and 45 with three-phase equilibrium regions inside the isothermal section. Fig. 16a shows the region connecting the three phases $Yb_2Zn_{17-x}Cu_x$, $YbZn_{11-x}Cu_x$ and γ, while Fig. 16b shows the three-phase region τ_2-$YbCu_{5-x}Zn_x$, $Yb_2Zn_{17-x}Cu_x$ and (Cu).

According to the literature, in the alloys of the Yb-Cu-Zn system with a composition ≥ 33 at% Yb, ytterbium with a valence of 2 + is present. This can be seen, for example, in Fig. 17, where the magnetic susceptibility of the compound Yb_5Cu_2Zn measured by Tappe *et al.* [19] is compared with the measurement of sample N. 15 ($Yb_{33}Cu_{50}Zn_{17}$), which belongs to the pseudobinary system $YbCu_2$-$YbZn_2$. In both cases, the low values of the susceptibilities indicate the Yb^{2+} valence. The Yb ion behaves in the same manner in YbZn and YbCu compounds. In fact, Iandelli and Palenzona reported an anomalous trend for R = Yb in the lattice parameters of CsCl-type RX compounds (R = rare earths, X = Zn and Cu), which is related to the valence of the Yb^{2+} ion [25].

On the other hand, with Yb compositions around 16.66 at%, the Yb valence depends on the crystal structure of the corresponding compound. Fig. 18 shows the χ(T) dependences for τ_1-$YbCu_{5-x}Zn_x$ ($0.7 \leq x \leq 1.0$) in the main panel compared to the values for τ_2-$YbCu_{5-x}Zn_x$ ($x = 2, 3, 4$) in the inset. While the magnitude of the values of magnetic susceptibilities in the inset of the figure is comparable to those in Fig. 17, much higher values of susceptibilities are measured for the τ_1-$YbCu_{5-x}Zn_x$ compositions of $AuBe_5$-type.

Fig. 19 shows the measurements of the inverse susceptibility 1/χ(T) of τ_1-$YbCu_{5-x}Zn_x$. The curves follow the Curie-Weiss (C-W) law for T > 50 K. The values of the effective magnetic moment μ_{eff} resulting from the fits of the C-W law are close to the expected values of the Yb^{3+} ion (4.54 μ_B). The inset shows the trend of 1/χ(T) for these compositions in the low-temperature range (2–40 K), with the negative curvature indicating the effect of thermal population reduction of the excited crystalline electric field (CEF) levels observed in similar Yb systems [3]. Table 6 lists the values of μ_{eff} and the paramagnetic temperature θ_p calculated at B = 1 T. The negative θ_p values, ranging from −30 K for $x = 0.70$ to −42 K for $x = 1.0$, indicate an antiferromagnetic character of the magnetic interaction, and the high absolute values of θ_p are similar to those obtained for the $YbCu_{5-x}Au_x$ system [3]. Since the literature reports for $YbCu_4Zn$ and $YbCu_{4.6}Au_{0.4}$ also a similar increase at low temperatures in both Cp/T and resistivity, measurements of low-temperature heat capacity and electrical resistivity are currently being performed for τ_1-$YbCu_{5-x}Zn_x$ to allow a comparison between the two systems $YbCu_{5-x}Au_x$ and τ_1-$YbCu_{5-x}Zn_x$.

The dependencies of the magnetization M(B) for the compositions τ_1-$YbCu_{5-x}Zn_x$ ($x = 0.7$) and τ_2-$YbCu_{5-x}Zn_x$ ($x = 3.0$) are compared (see Fig. 20). A significant difference in the absolute values between the

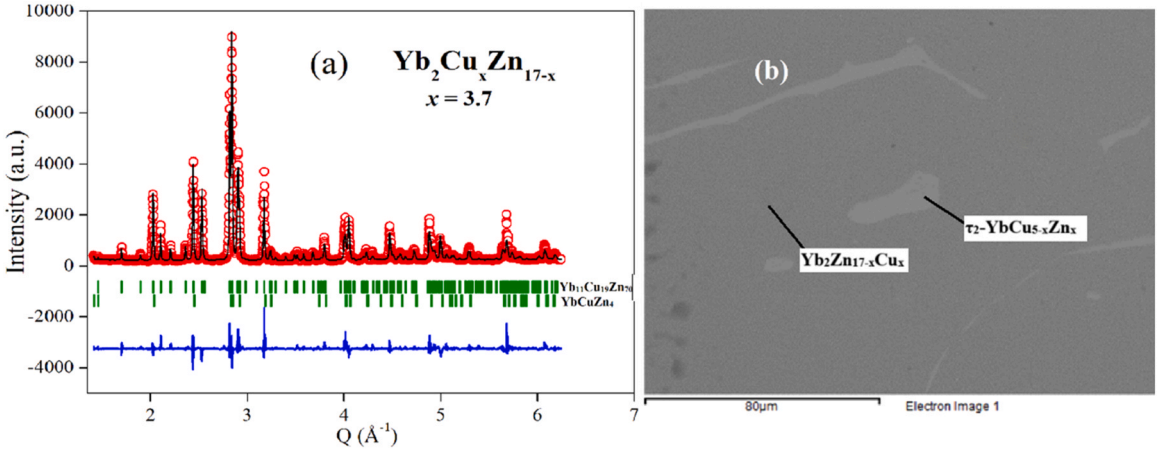

Fig. 15. (a) Rietveld refinement plot and (b) BSE image for sample N. 44 containing matrix: $Yb_2Zn_{17-x}Cu_x$ (x = 3.6); white phase: τ_2-$YbCu_{5-x}Zn_x$ (x = 4.0).

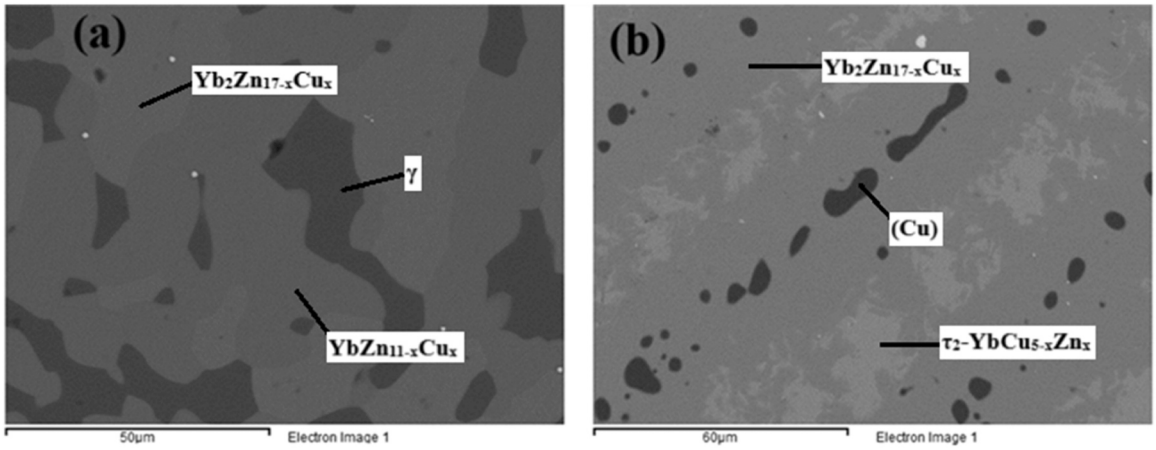

Fig. 16. BSE images of samples (a) N. 42 containing three phases: light gray: $Yb_2Zn_{17-x}Cu_x$ (x = 3.8); dark gray: $YbZn_{11-x}Cu_x$ (x = 2.2) and black: γ and (b) N. 45 containing three phases: matrix (dark gray) $Yb_2Zn_{17-x}Cu_x$ (x = 10.1), light gray: τ_2-$YbCu_{5-x}Zn_x$ (x = 1.9) and black: (Cu).

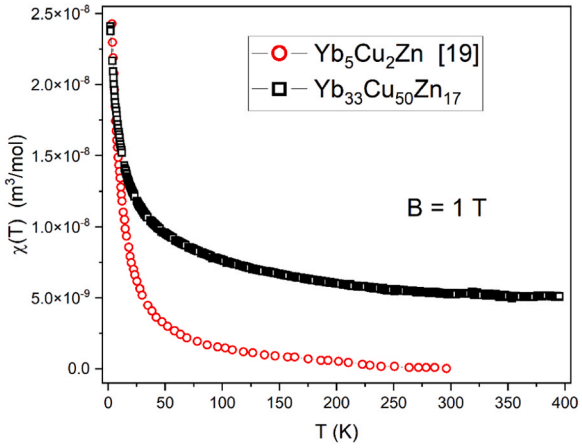

Fig. 17. Susceptibility χ(T) measurements at B = 1 T for Yb_5Cu_2Zn and $Yb_{33}Cu_{50}Zn_{17}$.

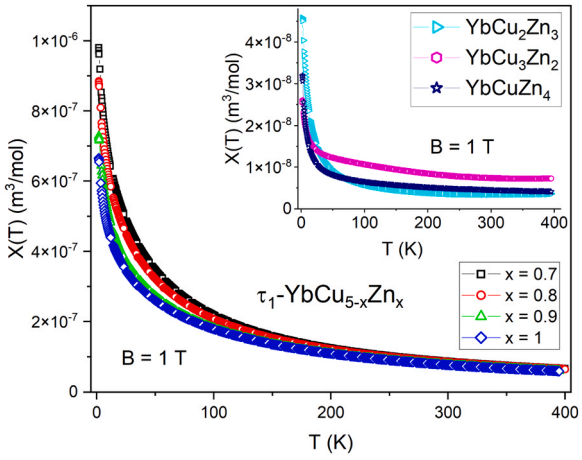

Fig. 18. Magnetic Susceptibility χ(T) measurements at B = 1 T for τ_1-$YbCu_{5-x}Zn_x$ (x = 0.7–1.0) vs τ_2-$YbCu_{5-x}Zn_x$ (x = 2, 3, 4) in the inset.

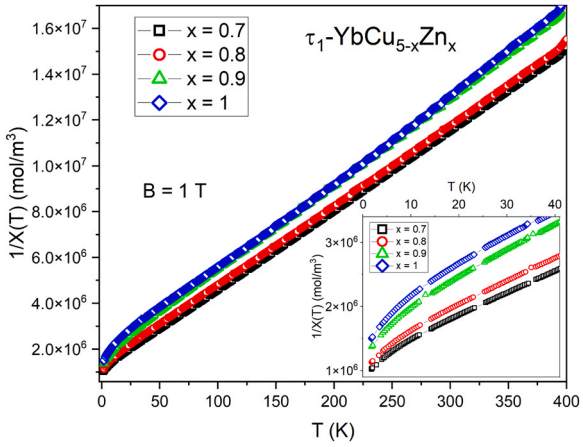

Fig. 19. Inverse susceptibility 1/χ(T) measurements at B = 1 T for τ_1-$YbCu_{5-x}Zn_x$ (x = 0.7–1.0); inset: low T values of 1/χ(T).

Table 6
Values of μ_{eff} and θ_p for τ_1-$YbCu_{5-x}Zn_x$ (x = 0.7–1.0) obtained from the C-W fit of the experimental data at B = 1 T.

B = 1 T	μ_{eff} (μ_B)	θ_p (K)
$x = 0.7$	4.27	-30
$x = 0.8$	4.25	-35
$x = 0.9$	4.11	-44
$x = 1$	4.08	-42

paramagnetic τ_1-$YbCu_{5-x}Zn_x$ ($x = 0.7$) and the nonmagnetic τ_2-$YbCu_{5-x}Zn_x$ ($x = 3.0$) compositions can be seen from the figure. This is consistent with the magnetic susceptibility measurements explained above (Fig. 17).

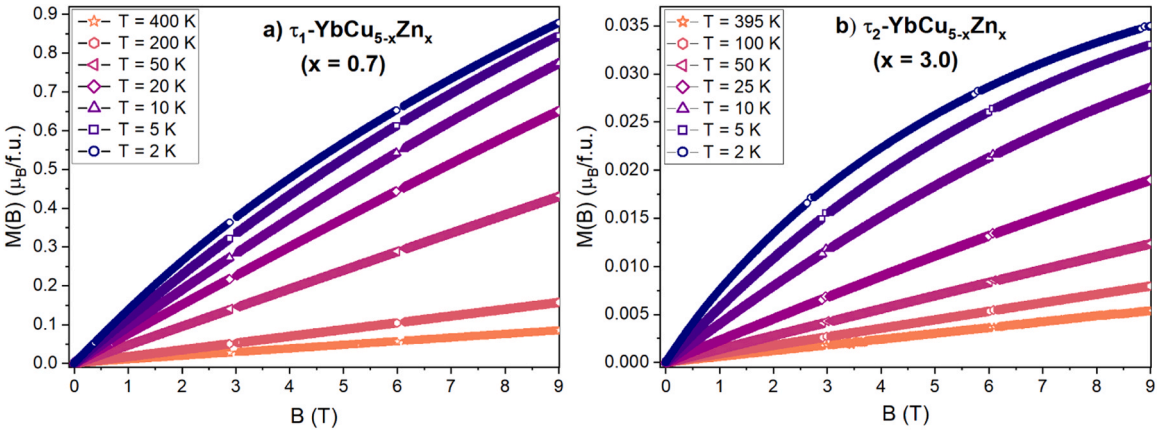

Fig. 20. Comparison of magnetization M(B) curves for (a) τ_1 (x = 0.7) and (b) τ_2 (x = 3.0).

5. Summary

Phase equilibria at 600 °C were studied for the Yb–Cu–Zn ternary system over the entire concentration range using XRD and SEM/EDXS analyzes. The isothermal section is characterized by phases with extended Cu/Zn solubility at constant Yb content, which are either formed from the Yb–Cu and Yb–Zn binary systems or exist in the ternary field.

Four ternary compounds are present in the Yb-Cu-Zn isothermal section: τ_1-$YbCu_{5-x}Zn_x$ (cubic $AuBe_5$ type, $0.4 \leq x \leq 1.5$), τ_2-$YbCu_{5-x}Zn_x$ (hexagonal $CaCu_5$ type, $1.8 \leq x \leq 4.4$), τ_3-Yb_2CuZn_7 and τ_4-$Yb_5Cu_{2-x}Zn_{1+x}$.

Unlike the Ce-Cu-Zn system, which exhibits an extended hexagonal $CeCu_{5-x}Zn_x$ solubility range of $CaCu_5$-type, the $YbCu_{5-x}Zn_x$ homogeneity region shows both the cubic $AuBe_5$-type and the hexagonal $CaCu_5$-type in different compositional regions, which affect the valence of the Yb ion. In fact, magnetic measurements revealed the magnetic Yb^{3+} state for τ_1: $x = 0.7$–1.0 while the nonmagnetic Yb^{2+} state was found for the composition τ_2: $x = 1.8$–4.4.

CRediT authorship contribution statement

Fiza Akbar: Data curation; Investigation; Writing – original draft, Formal analysis. **Ivan Curlik**: Investigation, Data curation, Validation. **Marian Reiffers**: Funding acquisition, Visualization; Validation. **Mauro Giovannini**: Conceptualization; Supervision; Writing – review & editing, Methodology, Writing – original draft.

Declaration of Competing Interest

The authors declare that they have no known competing financial interests or personal relationships that could have appeared to influence the work reported in this paper.

Data availability

Data will be made available on request.

Acknowledgments

This work results from the implementation of the following projects: University Science Park TECHNICOM for Innovation Applications Supported by Knowledge Technology – II – Phase, ITMS: 313011D232, supported by the Operational Programme for Research and Development, funded by the ERDF, and VEGA 1/0404/21.

References

[1] F. Steglich, S. Wirth, Foundations of heavy-fermion superconductivity: lattice Kondo effect and Mott physics, Rep. Prog. Phys. 79 (2016), 084502, https://doi.org/10.1088/0034-4885/79/8/084502.
[2] Vojta Matthias, Quantum phase transitions, Rep. Prog. Phys. 66 (2003) 2069, https://doi.org/10.1088/0034-4885/66/12/R01.
[3] I. Ćurlík, M. Giovannini, J.G. Sereni, M. Zapotoková, S. Gabáni, M. Reiffers, Extremely high density of magnetic excitations at T = 0 in $YbCu_{5-x}Au_x$, Phys. Rev. B 90 (2014), 224409, https://doi.org/10.1103/PhysRevB.90.224409.
[4] K. Yoshimura, N. Tsujii, J. He, M. Kato, K. Kosuge, H. Michor, K. Kreiner, G. Hilscher, T. Goto, Synthesis and dense kondo behavior of cubic $AuBe_5$-type $YbCu_5$ compound-systematic change of physical properties in the $YbCu_{5-x}Ag_x$ ($0 \leq x \leq 1$) system, J. Alloy. Compd. 262 (1997) 118–123, https://doi.org/10.1016/S0925-8388(97)00340-X.
[5] J. He, N. Tsujii, K. Yoshimura, K. Kosuge, T. Goto, Crossover from first-order valence transition to kondo behavior in C15b-type $YbCu_{5-x}In_x$ System, J. Phys. Soc. Jpn. 66 (1997) 2481–2486, https://doi.org/10.1143/JPSJ.66.2481.
[6] E. Bauer, R. Hauser, A. Galatanu, H. Michor, G. Hilscher, J. Sereni, M.G. Berisso, P. Pedrazzini, M. Galli, F. Marabelli, P. Bonville, Non-fermi-liquid behavior of $YbCu_{5-x}Al_x$, Phys. Rev. B 60 (1999) 1238, https://doi.org/10.1103/PhysRevB.60.1238.
[7] J. He, G. Ling, Z. Jiao, Magnetic and transport properties of cubic $AuBe_5$-type $YbCu_{5-x}Ga_x$ system, Phys. B Condens. Matter 301 (2001) 196–202, https://doi.org/10.1016/S0921-4526(00)00758-4.
[8] C. Rossel, K.N. Yang, M.B. Maple, Z. Fisk, E. Zirngiebl, J.D. Thompson, Strong electronic correlations in a new class of Yb-based compounds: $YbXCu_4$ (X=Ag,Au, Pd), Phys. Rev. B 35 (1987) 1914, https://doi.org/10.1103/PhysRevB.35.1914.
[9] J.L. Sarrao, C.D. Immer, Z. Fisk, C.H. Booth, E. Figueroa, J.M. Lawrence, R. Modler, A.L. Cornelius, M.F. Hundley, G.H. Kwei, J.D. Thompson, Physical properties of $YbXCu_4$ (X = Ag, Au, Cd, Mg, Tl, and Zn) compounds, Phys. Rev. B 59 (1999) 6855, https://doi.org/10.1103/PhysRevB.59.6855.
[10] A. Iandelli, A. Palenzona, Ytterbium–copper system, J. Less-Common Met. 25 (1971) 333–335, https://doi.org/10.1016/0022-5088(71)90158-5.
[11] Subramanian P.R., Laughlin D.E., 1994. Monograph series on alloy phase diagrams–phase diagrams of binary copper alloys, 10. pp. 482–486.
[12] M. Giovannini, R. Pasero, S. De Negri, A. Saccone, $Yb(Cu,T)_5$ and $Yb(Cu,T)_{4.5}$ solid solutions (T = Ag, Au, Pd), Intermetallics 16 (2008) 399–405, https://doi.org/10.1016/j.intermet.2007.11.010.
[13] B.B. Argent, D.W. Wakeman, Thermodynamic properties of solid solutions. Part 1-Copper+zinc solid solution, Trans. Faraday Soc. 54 (1958) 799–806, https://doi.org/10.1039/TF9585400799.
[14] T.B. Massalski, H. Okamoto, P. Subramanian, L. Kacprzak, W.W. Scott, Binary Alloy Phase Diagrams, American society for metals, Metals Park, OH, 1986.
[15] J.T. Mason, P. Chiotti, The ytterbium–zinc phase diagram, Trans. AIME 242 (1968) 1167–1171.
[16] G. Bruzzone, M.L. Fornasini, F. Merlo, Rare-earth intermediate phases with zinc, J. Less Common Met. 22 (1970) 253–264, https://doi.org/10.1016/0022-5088(70)90074-3.
[17] A. Iandelli, A. Palenzona, Zinc-rich phases of the rare-earth-zinc alloys, J. Less Common Met. 12 (1967) 333–343, https://doi.org/10.1016/0022-5088(67)90001-X.
[18] M.L. Fornasini, A. Iandelli, F. Merlo, M. Pani, Crystal structure of the RCuZn, RAgZn and RAgAl intermetallic compounds (R = rare earth metals), Intermetallics 8 (2000) 239–246, https://doi.org/10.1016/S0966-9795(99)00111-9.
[19] F. Tappe, C. Schwickert, M. Eul, R. Pöttgen, Intermetallic cadmium compounds M_5T_2Cd (M = Ca, Yb, Eu; T= Cu, Ag, Au) with Mo_5B_2Si-type Structure, Z. Naturforsch. B 66 (2011) 1219–1224, https://doi.org/10.1515/znb-2011-1204.
[20] W. Kraus, G. Nolze, POWDER CELL-a program for the representation and manipulation of crystal structures and calculation of the resulting X-ray powder patterns, J. Appl. Crystallogr. 29 (1996) 301, https://doi.org/10.1107/S0021889895014920.

[21] Laugier J., Bochu B.,1999. CELREF: Cell parameters refinement program from powder diffraction diagram. Laboratoire des Matériaux et du Génie Physique, Ecole Nationale Supérieure de Physique de Grenoble (INPG), Grenoble, France.
[22] J. Rodríguez-Carvajal, Recent advances in magnetic structure determination by neutron powder diffraction, Phys. B 192 (1993) 55, https://doi.org/10.1016/0921-4526(93)90108-I.
[23] V. Pavlyuk, W. Prochwicz, P. Solokha, O. Zelinska, B. Marciniak, E. Różycka-Sokołowska, Interaction of the components in the Ce-Cu-Zn ternary system at 200 °C, J. Alloy. Compd. 407 (2006) 226–231, https://doi.org/10.1016/j.jallcom.2005.06.057.
[24] V. Pavlyuk, E. Różycka-Sokołowska, B. Marciniak, W. Prochwicz, P. Solokha, P. Dzierżanowski, Structural study of the pseudobinary $CeCu_5$–$CeZn_5$ system, J. Alloy. Compd. 373 (2004) 137–141, https://doi.org/10.1016/j.jallcom.2003.10.028.
[25] A. Iandelli, A. Pallenzona, Atomic size of rare earths in intermetallic compounds. MX compounds of CsCl type, J. Less Common Met. 9 (1965) 1–6, https://doi.org/10.1016/0022-5088(65)90028-7.